Oxidation under air of tavorite LiVPO4F : influence of vanadyl-type defects on its electrochemical properties

Edouard Boivin, Jean-Noël Chotard, Michel Ménétrier, Lydie Bourgeois, Tahya Bamine, Dany Carlier, François Fauth, Christian Masquelier, Laurence Croguennec

Oxidation Under Air of Tavorite $LiVPO_4F$: Influence of Vanadyl-type Defects on its Electrochemical Properties

Edouard Boivin [a, b, f], Jean-Noël Chotard [b, f, g], Michel Ménétrier [a, f], Lydie Bourgeois [c, d], Tahya Bamine [a, f], Dany Carlier [a, f], François Fauth [e], Christian Masquelier [b, f, g] and Laurence Croguennec [a, f, g,*]

[a] *CNRS, Univ. Bordeaux, Bordeaux INP, ICMCB UPR 9048, F-33600 Pessac, France.*

[b] *Laboratoire de Réactivité et de Chimie des Solides, CNRS-UMR#7314, Université de Picardie Jules Verne, F-80039 Amiens Cedex 1, France.*

[c] *Université de Bordeaux, ISM, Groupe de Spectroscopie Moléculaire, F-33405 Talence, France.*

[d] *Bordeaux INP, ISM, CNRS, UMR 5255, F-33405, Talence, France.*

[e] *CELLS - ALBA synchrotron, E-08290 Cerdanyola del Vallès, Barcelona, Spain.*

[f] *RS2E, Réseau Français sur le Stockage Electrochimique de l'Energie, FR CNRS 3459, F-80039 Amiens Cedex 1, France.*

[g] *ALISTORE-ERI European Research Institute, FR CNRS 3104, F-80039 Amiens Cedex 1, France.*

[*] Corresponding author (L. Croguennec): Laurence.Croguennec@icmcb.cnrs.fr

Abstract

Tavorite-type compositions offer a very rich crystal chemistry, among which $LiV^{III}PO_4F$ has the highest theoretical energy density (*i.e.* 655 Wh/kg). In this article, an in-depth study of vanadyl-type defects generated by temperature-controlled oxidation of $LiV^{III}PO_4F$ under air is proposed and their influence on the electrochemical properties are demonstrated. A combination of high resolution synchrotron diffraction, infrared spectroscopy and magic angle spinning nuclear magnetic resonance was used to fully characterize the materials thus generated, from their average long range structure to their local structure with the presence of defects. The increase of the annealing temperature tends to substitute oxygen for fluorine with the formation of a series of $LiVPO_4F_{1-x}O_x$ compositions. The miscibility domains appear to be narrow at the two ends of the solid solution (*i.e.* in the composition ranges $LiVPO_4F_{[1 - 0.9]}O_{[0 - 0.1]}$ and

$LiVPO_4 F_{[0 - 0.1]}O_{[1 - 0.9]}$). The presence of vanadyl-type defects obtained as localized or more extended ones, depending on the annealing conditions, affects drastically the electrochemical properties of these Tavorite $LiVPO_4F$-type materials.

Introduction

The increasing mobility of populations and the need to fight against global warming with the development of sustainable energies are two reasons for which electrochemical energy storage is one of the major issue for scientific researches both at the academic and industrial levels. The Lithium-ion battery technology is already largely used as an energy source for mobile devices such as smartphones, laptops etc. Nevertheless, for applications such as electric and hybrid vehicles, the energy density delivered by these batteries cannot currently compete with fossil energy (cost and limited autonomy in particular). Polyanionic compounds could be promising candidates at the positive electrode of Lithium-ion batteries developed for that kind of applications, due to higher working potential for a given $M^{n+}/M^{(n-1)+}$ redox couple than in oxides [1] and, for some of them, higher chemical and thermal stability. Among them, A_xMXO_4Y Tavorite-type compounds (with A = Li, Na, … ; M= Ti, V, Mn, Fe, … ; X = P or S and Y = O, OH, F and mix of them) are of interest [2–4]. MO_4Y_2 octahedra are linked by bridging anions Y to form infinite chains $[Y\text{-}MO_4\text{-}Y]_n$ which are connected by XO_4 polyanionic groups in such way that each oxygen atom belongs to one different octahedron. The three dimensional network thus generated can accommodate alkaline cations which can diffuse easily. The Tavorite framework is tailored according to the inductive effect coming from the bridging anion Y (O, OH or F) in addition to that from the XO_4 polyanionic group. The environment of the transition metal thus greatly influences the potential of the redox couple involved. Typically, for the same redox couple Fe^{III}/Fe^{II}, lithium insertion occurs at a potential of 2.6 and 2.9 V vs Li^+/Li in $LiFe^{III}PO_4OH$ [5] and $LiFe^{III}PO_4F$ [6], respectively. Indeed, fluorine is more electronegative than the hydroxyl group, inducing the formation of a more ionic metal-ligand bond, a decreasing energy of the antibonding orbital level, and thus an increasing potential difference of the Fe^{III}/Fe^{II} redox couple versus Li^+/Li.

Vanadium based phosphate Tavorite compounds are very attractive because of their high potential and theoretical energy density, at least competitive with the already commercialized $LiFePO_4$ [2]: 655Wh/Kg of theoretical energy density for $LiVPO_4F$ vs. 586Wh/Kg for

$LiFePO_4$. $LiVPO_4F$ is generally synthesized using a lengthy two steps ceramic synthesis route [7,8] and most of the efforts currently devoted to this material are focused on the development of an easy, eco-friendly and scalable synthesis process maintaining optimal electrochemical properties [9]. Nevertheless, among the huge number of articles (over 100) which report on an apparently pure $LiVPO_4F$ there are significant differences in lattice parameters and unit cell volumes that fluctuate for these latter between V/Z = 87.00 [10] and V/Z = 87.31 $Å^3$ [11] whereas the difference between $LiVPO_4O$ (V/Z = 85.51 $Å^3$ [8]) and $LiVPO_4F$ is around 1.7 $Å^3$. Indeed, some of us have shown that apparently pure and stoichiometric $LiVPO_4F$ powders, as determined from X-ray and neutron diffraction as well as high resolution transmission electron microscopy, surprisingly contain a series of local defects detected by ^{7}Li Magic Angle Spinning Nuclear Magnetic Resonance spectroscopy (MAS NMR) [12]. In parallel to the presence of these defects, slightly different electrochemical signatures were observed as revealed by their irreversible capacity, reversible capacity and polarization [12,13]. The amount of these defects varies and could result from a partial oxidation during the synthesis or the storage. The study of $LiVPO_4F$ thermal stability in air was reported in reference [14] and raised interesting questions concerning the nature of the possible defects formed and their influence on the electrochemical properties.

In the following we will describe the oxidation of $LiVPO_4F$ performed in similar conditions to those reported by Ma *et al.* [14], and its effect on the composition, structure and electrochemical properties. We will show that combination of Synchrotron X-ray powder diffraction with Infra-Red and NMR spectroscopies is essential to identify the nature of the phases and local defects formed, and to understand in-depth the electrochemical behavior observed in lithium batteries.

1. Experimental part

The pristine material, $LiVPO_4F$, was synthetized, according to the reaction (1) through a two steps carbothermal reduction, as described previously [7,8]. V_2O_5 (Sigma-Aldrich, > 98%) is reduced by a small excess of C_{SP} carbon (*i.e.* a highly divided soot) in the presence of $NH_4H_2PO_4$

(Sigma-Aldrich, > 99%). A thermal treatment at 800°C under argon flow leads to the formation of VPO_4/C, in which the vanadium phosphate particles are surrounded by residual carbon nanoparticles localized in the grain boundaries. After the addition of a stoichiometric amount of LiF to VPO_4/C, the mixture is annealed at 800°C under argon flow to form $LiVPO_4F$. $LiVPO_4O$ was also synthetized by a solid state reaction from V_2O_3 (Cerac, ≤ 99.9%), Li_3PO_4 (Sigma-Aldrich, 97%) and $NH_4H_2PO_4$ (Sigma-Aldrich, > 99%) as described in reference [8] and according to the reaction (2).

(1) Step 1 $V^{V}{}_2O_5 + 2\ NH_4H_2PO_4 + 2C + C_{excess} \rightarrow 2\ V^{III}PO_4/C + 2\ NH_3 + CO_2 + CO + 2\ H_2O$

Step 2 $V^{III}PO_4/C + LiF \rightarrow LiV^{III}PO_4F/C$

(2) $V^{III}{}_2O_3 + 4/3\ NH_4H_2PO_4 + 2/3\ Li_3PO_4 + ½\ O_2 \rightarrow 2\ LiV^{IV}PO_4O + 4/3\ NH_3 + 2\ H_2O$

The thermogravimetric analysis (TGA) of the pristine material $LiVPO_4F$ was performed on a TA instruments Q600 under air and over a temperature range between 20 and 700°C, with a continuous heating rate of 5°C/min for the first experiment. In order to separate the different weight losses and overpass the kinetics phenomena, then several plateaus were performed during 30 minutes at the characteristic temperatures defined by the first experiment (*i.e.* 450, 525, 600 and 700°C).

Based on TGA results, a series of oxidized materials were prepared by heating the pristine material $LiVPO_4F$ at different temperatures (T = 375, 450, 525, 600 and 700°C) during 30 minutes under air in a muffle furnace and then by quenching them under air. In the following, the resulting samples are called as LVPF-T in general or LVPF-375, LVPF-450, ... to specify the in-air treatment temperature. Note that the storage of these samples is a key parameter in order to avoid any evolution of the samples over time, we thus kept them in an Argon filled glove box ($[H_2O]$ < 1 ppm and $[O_2]$ < 1 ppm) as much as possible.

In order to confirm the chemical compositions of the samples, the Li, V, and P contents were determined using an Inductively Coupled Plasma / Optical Emission Spectrometry (ICP-OES) spectrometer (Varian 720-ES Optical Emission Spectrometer) after complete dissolution of

the powders into a mixture of hydrochloric and nitric acids. Elemental analyses of C and H were performed using a gas chromatography spectrometer, an Elementar Vario Micro Cube CHNS.

The investigation of the morphology was performed by Scanning Electron Microscopy (SEM) using a Hitachi S-4500 microscope. The powders were previously metallized by gold deposition.

High angular resolution Synchrotron X-ray powder diffraction (SXRPD) experiments were performed at the MSPD beamline of the ALBA synchrotron[15] (Barcelona, Spain). Data were collected using the MYTHEN position sensitive detector in Debye-Scherrer geometry, at 0.9539 Å wavelength, over a 2° - 72° angular range (0.006° step) and total integration time of 5 minutes. The samples were sealed in a 0.5 mm diameter capillary. Diffraction data analysis was performed using the FullProf Suite [16]. The profile of the diffraction lines of the highly defected materials had to be fitted using a phenomenological anisotropic strain broadening model [17,18] after deconvolution of the instrumental contribution determined from a silicium reference. The structural model is described within a triclinic unit cell with 18 independent atoms, leading hence to a large number of refined parameters: up to 104 for a single phase model, 212 for some of $LiVPO_4F$-T compounds exhibiting two coexisting phases. For these reasons, Rietveld refinements were performed applying soft constraints on P-O distances (1.55 Å ± 0.05) and O-P-O angles (109.5° ± 2.50) to describe the covalent $\{PO_4\}^{3-}$ anionic groups.

In order to support the composition and the structure of the different materials studied, magic angle spinning nuclear magnetic resonance (MAS NMR) was performed. ^{7}Li MAS NMR spectra were recorded on a 300 MHz Bruker Avance spectrometer with a 7T magnet (116 MHz resonance frequency), using a standard Bruker 2.5 MAS probe at a 30 kHz typical spinning speed. A Hahn echo sequence was applied with a 90° pulse of 1.2 µs for the probed nucleus. The relaxation time (D1) was 100s and the 0 ppm external reference was a 1M LiCl aqueous solution. ^{31}P MAS NMR spectra were recorded on a 100 MHz Bruker Avance III spectrometer with a 2.35T magnet (40.6 MHz Larmor frequency), a standard Bruker 2.5 MAS probe at a 30 kHz typical spinning speed. A Hahn echo sequence was used with a 90° pulse of 1.2 µs with a relaxation time of 1s. The 0 ppm external reference was a 1M H_3PO_4 aqueous solution. ^{19}F MAS NMR spectra were recorded on a Bruker Avance III spectrometer with a 2.35T magnet (94.3 MHz

resonance frequency for ^{19}F), using a standard Bruker 2.5 MAS probe at a 30 kHz typical spinning speed. A Hahn echo sequence was used with a 90° pulse of 1 microsecond. A recycle delay of 1s was applied. The 0 ppm external reference was $CFCl_3$.

Infrared spectroscopy measurements were performed in the range of 400−4000 cm^{-1} (mid-IR) using a FTIR Nicolet 6700 (Thermo Scientific) equipped with a DTGS detector and a diffuse reflectance accessory. The samples were finely ground in a mortar with dried KBr, the mass ratio between active material and KBr being approximately 1:50. Finally, reflectance spectra were treated with the Kubelka-Munk law, which converts the reflectance to a signal proportional to the absorption coefficient.

The electrochemical tests were carried out in lithium coin cells. The electrodes were prepared using 80 wt% of active material, 10 wt% of carbon (Super P) taking into account the remaining carbon from synthesis and 10 wt% of polyvinylidene fluoride (PVDF). N-methyl pyrrolidone was added to this mixture and the resultant slurry was cast on an Al foil and dried at 60°C during 24h. Discs (diameter 12 mm) were cut in this foil and after a day of drying at 80°C under vacuum, these electrodes were cycled in coin cells vs. metallic Lithium in galvanostatic mode at a rate of C/50 and C/10. The electrolyte used was a 1M solution of $LiPF_6$ in ethylene carbonate and dimethyl carbonate in a 1:1 volume ratio (LP30). Lithium cells were cycled, either in the high voltage domain between 3.0 and 4.6 V vs Li^+/Li or in the low voltage domain between 3.0 and 1.5 V vs Li^+/Li.

2. Results and discussion

2a. Samples preparation and their structural study

As illustrated in **Figure 1**, $LiVPO_4F$ was obtained as pure: all the diffraction lines could be indexed in a typical Tavorite unit cell described in the P-1 space group with a = 5.16893(3) Å, b = 5.30867(3) Å c = 7.26212(3) Å, α = 107.591(4)°, β = 107.972(5)°, γ = 98.394(4) ° and V/Z = 87.18 $Å^3$. The refinement by the Rietveld method of the structure of $LiVPO_4F$ confirms the

description already reported by Ateba Mba et al. [8], *i.e.* the formation of a three dimensional network with a single crystallographic site for the Li^+ ions.

The TGA data obtained for the thermal treatment of $LiVPO_4F$ under air (**Figure 2**) highlights three weight-loss domains. The first one, between 25°C and 100°C, matches with the evaporation of the adsorbed water and corresponds to about 0.2 wt.%. The second one starts at 375°C and is associated to a weight loss of 6 wt. % (until 450°C) that may correspond to the elimination of the surrounded carbon through the formation of CO_2 (*i.e.* approximately to the 5 wt.% of carbon remaining in the coated $LiVPO_4F$). The third transition occurs near 525°C and generates a loss of 1.7 wt. % of the initial mass, which would correspond to the weight loss expected for a complete substitution of oxygen for fluorine. Note that the oxidation of $LiVPO_4F$ may begin at lower temperature. A small weight gain occurs (around 0.5 wt.%) upon heating from 600°C to 700°C that is lost upon cooling. The XRD pattern of the material recovered at the end of this thermal treatment under air corresponds to that of the Tavorite phase $LiV^{IV}PO_4O$ with $Li_2V^{V}PO_6$ present as a minor impurity (most probably at the origin of this reversible weight gain). In order to get more insight into the nature of the materials successively formed during the thermal treatment under air, a series of controlled thermal treatments of the pristine material, $LiVPO_4F$, was performed under air during 30 minutes at various annealing temperatures. The six samples thus obtained are called in the following LVPF-T (with T= 375, 450, 525, 600 and 700°C).

Selected 2θ domains of Synchrotron XRD patterns of these samples are compared in **Figure 3**, with the corresponding SEM images given in inset. A rather continuous evolution of the diffraction patterns is observed. Contrary to the results obtained by Ma *et al.* [14], a clear phase separation is observed for samples thermally treated at 525°C and above. For the lower temperature treated samples (*i.e.* up to 450°C), no obvious significant change of the diffraction pattern is observed though a very narrow solid solution domain seems to be formed. For the high temperatures processed samples, the XRD patterns could appear as a combination of LVPF and LVPO ones. The SEM images associated to LVPF reveals the formation of aggregates made of 300-600 nm primary particles with 20 nm divided carbon at their surface (the latter appearing

as bright small particles in **Figure 3**). The SEM images also highlight the almost complete disappearance of carbon nanoparticles at 450°C, in good agreement with the TGA analysis. Furthermore, a significant increase of the particles size is observed from 300 - 600 nm for the pristine LVPF material to 1000 - 5000 nm for LVPF-700. Curiously, this growth of particles is not accompanied by a narrowing of the diffraction lines. In fact, the formation of highly defected materials and/or the separation into phases very close in compositions are likely at the origin of strain induced peaks broadening.

ICP-OES and CHNS analyses of these samples were carried out in order to titrate the Li, P and V contents on one side and the remaining carbon on the other side, and to check for the chemical composition of these materials. **Table 1** summarizes the results obtained. As expected by TGA results, a volatilization of remaining carbon as CO_2 is observed mostly between LVPF-450 and LVPF-525. This observation is supported by the change in the color of the different samples, from dark grey for LVPF-375 to brown for LVPF-525 and green for LVPF-700. Raman spectroscopy is one of the most sensitive techniques to characterize carbonated systems and was used to follow the carbon content of LVPF-T materials. As shown in supplementary information (in **Figure S1**), Raman bands observed in the 1200 - 1700 cm^{-1} range are assigned to sp^2-hybridized and disorder-induced lines of carbon systems. The evolution of their integrated intensity can be related to that of the carbon amount. Raman measurements reveal a strong decrease of the carbon content with the increasing annealing temperature, but also the presence of residual carbon until 525°C, in agreement with CHNS results. Contrary to the results reported by Ma *et al.* [14], no significant variation of the Li/V ratio from 1/1 is observed (neither for the Li/P ratio nor for the V/P ratio) suggesting that the stoichiometry $LiVPO_4Y$ ($Y = F_{1-x}O_x$) is maintained.

In order to ascertain the nature of the materials formed following our in-air thermal treatment, corresponding XRD patterns were analyzed and structural models were refined by the Rietveld method considering either a single or two Tavorite-type phases : $LiVPO_4F$-type or/and $LiVPO_4O$-type. The main difference between $LiV^{III}PO_4F$ and $LiV^{IV}PO_4O$ lies in the distances observed along the chains of octahedra [8]: they are constant and equal to 1.98 Å in $LiVPO_4F$, whereas there is an alternation between a short bond (the vanadyl bond around 1.7 Å) and a

longer bond (around 2.2 Å) in $LiVPO_4O$. In $LiVPO_4F$ the vanadium cations are thus sitting at the center of the VO_4F_2 octahedra, in special positions $(0, 0, 0)_{P\text{-}1}$ and $(0, 0, 1/2)_{P\text{-}1}$. In order to allow the displacement of the vanadium cations from the center of the octahedra along the chains, and the possible formation of oxy-fluoride $LiVPO_4F_{1-x}O_x$ solid solutions, the Rietveld refinements were performed considering a $LiVPO_4O$-type model, and thus the doubling of the unit cell according to the following matrix:

$$\begin{Bmatrix}\vec{a}\\ \vec{b}\\ \vec{c}\end{Bmatrix}_{LVPO} = \begin{Bmatrix}1\,0\,1\\ 1\,0\,\overline{1}\\ 0\,1\,0\end{Bmatrix} * \begin{Bmatrix}\vec{a}\\ \vec{b}\\ \vec{c}\end{Bmatrix}_{LVPF}$$

Described in a $LiVPO_4O$-type model the cell parameters of $LiVPO_4F$ are a = 6.84751(3) Å, b = 7.26212(3) Å, c = 7.93166(3) Å, α = 89.931(4) °, β = 91.544(5) °, γ = 117.854(4) ° and V/Z = 87.18 $Å^3$. The results of the refinements are summarized in **Table 2** and in the **Figures 4** and **5**. The patterns of LVPF-375 and LVPF-450 (as highlighted for the latter in **Figure 4a**) can be refined using a single phase model, close to LVPF but significantly different, revealing thus that a solid solution domain exists below 450°C. For instance, the V/Z values obtained for LVPF-375 and LVPF-450 are 87.12 $Å^3$ and 87.05 $Å^3$ respectively, versus 87.18 $Å^3$ for LVPF. In order to estimate the substitution level in these materials the Vegard's law was applied on their volumes,their vanadium average oxidation states would be 3.02 and 3.05 respectively, versus 3 for LVPF, hence their compositions would be $LiVPO_4F_{0.98}O_{0.02}$ and $LiVPO_4F_{0.95}O_{0.05}$. Note that the individual cell parameters don't follow this law and a strong deviation is observed, especially for a and b parameters (see **Figure S2** in supplementary information). As reported before in [19], single crystals with $LiVPO_4F_{1-x}O_x$ compositions also doesn't adopt a linear evolution of their cell parameters with the substitution ratio whereas the cell volume does. The formation of the vanadyl bond (along the b axis) may be disrupted by the presence of antagonist fluorine and the resultant distances in these $^{\cdots}F\text{--}V^{IV}\text{=}O\text{--}V^{III}\text{-}F^{\cdots}$ sequences would be different to the average of $F\text{-}V^{III}\text{-}F$ and $O\text{-}V^{IV}\text{=}O$ bond lengths in end-member phases. In that case, the oxygen-fluorine repartition along the chains may have a strong influence. Nevertheless, diffraction techniques are unable to determine this repartition. From 525°C two phases are observed in each sample, and must be considered for the Rietveld refinement to determine their structure (as highlighted

for LVPF-525 in **Figure 4b**). Both Tavorite-type phases belong to the $LiVPO_4F_{1-x}O_x$ phase diagram, one is close to LVPF whereas the other is close to LVPO. Their compositions are $LiVPO_4F_{0.90}O_{0.10}$ and $LiVPO_4F_{0.08}O_{0.92}$ respectively. The refinements of LVPF-600 and LVPF-700 confirm the persistence of the phase separation, but at higher treatment temperatures the Tavorite-type phases formed are really close to LVPO (*i.e.* $LiVPO_4F_{0.11}O_{0.89}$ and $LiVPO_4F_{0.03}O_{0.97}$ for LVPF-600 and $LiVPO_4F_{0.04}O_{0.96}$ and $LiVPO_4F_{0.01}O_{0.99}$ for LVPF-700). The global compositions calculated for each sample, taking into account the composition and weight percentage determined for each phase, are continuously enriched in oxygen with the increase in the annealing temperature moving from $LiVPO_4F_{0.96}O_{0.04}$ for LVPF-375 to $LiVPO_4F_{0.02}O_{0.98}$ for LVPF-700. Moreover, as the substitution of oxygen for fluorine increases, the average oxidation state of vanadium increases and the difference between the short and the long V-X bonds increases along the chains, from 0.04 Å for LVPF to 0.65 Å for LVPF-700 (**Table 2** and **Figure 5a**), in good agreement with the formation of more and more vanadyl-type bonds along the chains. Note that the length of the short bond decreases faster than the long one grows. Furthermore, these changes are not linear with an increasing substitution of oxygen for fluorine. This could be also in relation with the deviation from the Vegard's law, mentioned above.

Due to an inhomogeneous line broadening, all these patterns were refined using an anisotropic strain broadening model, corresponding to a P-1 space group and provided in the Fullprof software [17,18]. By drawing the so called Williamson-Hall plot (*i.e.* $\beta_{obs}.\cos\Theta$ as function of $\sin\Theta$), the size and strain effects can be separated. **Figure 5b** shows the evolution of the width of the microstrains' distribution ($\varepsilon_{hkl} = \Delta d_{hkl}/d_{hkl}$) along peculiar directions ([100], [010], [001] and in average along all [hkl] directions) for all samples and **Table 2** summarizes the microstructure parameters (D_{hkl} (= the apparent crystallite size) and ε_{hkl}).

The analysis of the microstructure reveals that the strains along these three directions increase until 525°C and then decrease gradually. Partial oxidation of the pristine material leads to the formation of vanadyl-type defects that would generate strains at the local scale, relaxed then thanks to the phase separation between a fluorine-rich phase and an oxygen(vanadyl)-rich phase. Moreover, the strains appear more extended along the [100] and [010] directions, this latter corresponding to the vanadyl bond propagation direction. Indeed, the substitution of a

part of fluorine by oxygen, leads to the formation of vanadyl bonds at the local scale (as dilute defects for small substitution ratios) which may disrupt the antagonist V-F bonds and generates small variations in the lattice parameters from one unit cell to another, especially along the b axis. The coherent diffraction size domains obtained from the microstructure analysis are consistent, from the pristine LVPF to LVPF-450, with the particles sizes observed by SEM and thus with a particles' growth most probably due to the effect of sintering. Then, a decrease of the apparent crystallites sizes is determined from 450°C to 525°C sample treatment, in parallel to a strong increase of microstrains, whereas an obvious particles' growth is observed by SEM. The intergrowth of different phases (here two, in a ratio close to 40:60 in LVPF-525 as reported in **Table 2**) inside the particles would induce the formation of multiple domains and boundaries resulting in the lowering of apparent crystallites sizes and in a strong increase of microstrains. At higher treatment temperature the narrowing of the diffraction lines is due to the combined effect of decreasing microstrains and increasing crystallites domain sizes generated by the sintering.

These results demonstrate the possibility to prepare phosphate Tavorite-type materials $LiVPO_4F_{1-x}O_x$, being mixed oxy-fluorides and showing thus mixed V^{3+}/V^{4+} valences. Nevertheless, it appears that, at least by this synthesis method *i.e.* an oxidation in temperature of $LiVPO_4F$, the solid solution domains are limited (with 10% of maximum substitution). The microstructure analysis reveals also the presence of size and strains effects in all these $LiVPO_4F_{1-x}O_x$, materials probably due to the large difference in nature between the bond sequences $O....V^{IV}=O$ and $F\text{-}V^{III}\text{-}F$ that makes difficult to mix them homogeneously/statistically along the chains. In addition to the average structural description given by X-ray diffraction, MAS NMR and IR spectroscopy appear as the most suitable complementary techniques to get an in-depth characterization of the local scale.

2b. Spectroscopic study

NMR

^{7}Li, ^{31}P, ^{19}F MAS NMR experiments were carried out on $LiVPO_4F$, $LiVPO_4O$ and all the annealed samples. This technique is sensitive to the local environment of the probed atom (nucleus) and proved to be a powerful tool to detect vanadyl-type defects [12].

Figure 6a shows the ^{7}Li MAS NMR spectra recorded for all samples. A rather sharp signal centered at 115 ppm is observed for $LiVPO_4F$, which is close to that published previously as corresponding to the unique Li site identified by diffraction [12,20]. The spectrum for the LVPF sample also exhibits a weak signal at -1 ppm assigned to the presence of residual LiF and others additional signals at 4, 84 and 186 ppm. 2D dipolar homonuclear correlation NMR experiments recently performed by Messinger et al. [12] have shown that all these additional signals are correlated to the main one, and correspond thus to Li^+ ions in the same material, that would be located nearby V ions with altered oxidation and/or spin states.. All paramagnetic materials (such as Vanadium based Tavorite-like compounds discussed in this section) lead to NMR spectra dominated by interactions between nuclear and electron spins (hyperfine interactions). The Fermi contact shift, which governs the position of the NMR signal of such compounds, corresponds to the presence of some density of electron spin at the nucleus probed. Indeed, the value of the Fermi contact shift is proportional to the spin density at the site of the probed nucleus and to the magnetic susceptibility of the compound [21]. Modelling of the defect in $LiVPO_4F$ considering the presence of oxygen replacing fluorine locally in the structure using DFT calculations, leads to a rather good ^{7}Li NMR signal assignment[22].

The investigation of the NMR spectrum of LVPO shows a single sharp peak at 79 ppm, less shifted than in $LiVPO_4F$ (115 ppm) due to the higher oxidation state of vanadium. Indeed, V^{4+} ($t_{2g}^{1}e_g^{0}$) provides less spin transfer towards the Li nuclei than V^{3+} ($t_{2g}^{2}e_g^{0}$), in the same structural environment. In $LiVPO_4O$, there are two crystallographic sites for Lithium [8]. So, two ^{7}Li MAS NMR peaks would have been expected whereas only one is detected, due to the strong structural and electronic similarity between the two sites as confirmed by the calculated shifts for the Li in the structure (see **Table S1** in supplementary information).

The effect of annealing treatment under air is detected as soon as 375°C. Indeed, for this sample a small decrease in intensity of the $LiVPO_4F$-type main signal is observed, with the appearance of a tiny peak at 80 ppm. This latter contribution seems to match with an $LiVPO_4O$-

type environment for Lithium. This trend is confirmed with an increase of the annealing temperature (*i.e.* 450°C and 525°C). Indeed, the intensity of the $LiVPO_4F$-type signal decreases at the benefit of the $LiVPO_4O$-type one. The NMR shifts are highly sensitive to the local environment of the probed nuclei and highlights thus here that only one additional environment can be detected for lithium, slightly different from that of $LiVPO_4O$ with an NMR shift 5 ppm smaller. Note that the $LiVPO_4F$-type contribution is slightly more shifted (116 ppm against 115 ppm for the pristine LVPF), that could be accounted for by a shortening of the Li-V distance due to the oxidation of vanadium in the vicinity of LVPF local type environments. Note also that there is a strong modification of the ^{7}Li MAS NMR spectra between LVPF-450 and LVPF-525, in good agreement with the results obtained by SXRD which highlight a weak substitution level of oxygen for fluorine in LVPF-450 (less than 10%) and a larger one for LVPF-525 with a global composition of $LiVPO_4O_{0.65}F_{0.35}$. For this latter and especially for LVPF-600, several new peaks appear and a significant broadening is observed. This is likely due to the formation of a series of different (V^{4+}, V^{3+}) environments for the Li^{+} ions in these materials highly disordered. Note that the appearance of these new contributions is done at the expense of those existing in the pristine material (4 and 186 ppm), the latter being associated with localized vanadyl-type defects[22]. Nevertheless, the correlation between these NMR shifts and the nature of the defects formed due to a partial oxidation of LVPF is not trivial and would require DFT calculations.

LVPF sample exhibits a single relatively sharp ^{31}P MAS NMR signal at 3998 ppm (**Figure 6b**) in agreement with the unique phosphorous site present in the structure. The two signals at 1593 ppm and 1418 ppm observed for $LiVPO_4O$ confirm the existence of two different types of phosphorus, in agreement with the two crystallographic sites. Based on the theoretical calculated shifts, the 1593 ppm shift is assigned to P1 and the 1418 ppm to P2 site (see **Table S1** in supplementary information). Furthermore, due to the smaller number of electrons in V^{4+} t2g orbitals of LVPO compared to that in V^{3+} t2g orbitals of LVPF, the isotropic signals in LVPO are less shifted than in LVPF. The effects of annealing on the ^{31}P MAS NMR spectra of the different samples is detected from 375°C with a slight decrease of the $LiVPO_4F$-type signal without any modification of its shift. At this temperature no new signal is observed. A small $LiVPO_4O$-type contribution is detected only from 450°C, with an NMR shift smaller than those observed for

LVPO (1365 and 1580 ppm against 1593 and 1418 ppm for LVPO). In this sample, the shift of the LVPF-type contribution is also affected, it increases from 3868 ppm for the pristine phase LVPF to 3911 ppm for LVPF-450. At 525°C, in the LVPO region, a new broad signal is observed around 2100 ppm. The shift of this peak is very different from those of LVPO and may correspond to a strongly disordered LVPO-type phase. This trend is amplified with the increase of the annealing temperature, indeed at 600°C this new contribution is even more intense: two components can be identified at 1930 and 2185 ppm, but a large contribution is also observed on the left. These signals are probably due to phosphorus nuclei in interaction with several distribution of V^{3+} and V^{4+} cations in their environment. The ^{31}P NMR spectrum of the sample annealed at 700°C is very close to that of LVPO, but it differs slightly in the shift (1413 and 1493 ppm versus 1443 and 1614 ppm for LVPO) and in the relative intensity of each signal. The diffraction analysis has shown that this material is a biphasic one, with two phases very close to each other, which could not be separated by ^{31}P MAS NMR. Furthermore, signal corresponding to phosphorus in diamagnetic compound grow at -9 and 52 ppm from 600°C.

The comparison of the ^{19}F MAS NMR spectrum of LVPF with those of the series of samples LVPF-T is given in supplementary information (**Figure S3**). The isotropic peak is located at -1500 ppm for LVPF. The global intensity of this signal decreases gradually until 700°C due the replacement of oxygen for fluorine and, surprisingly, no others peaks which would be assigned to Fluorine atoms in interaction with V^{4+} cations can be detected. The large number of spinning sidebands and the narrow solid solution domains (with less than 10% of oxygen substitution for fluorine (and vice versa) in $LiVPO_4F_{1-x}O_x$) could make difficult the observation of the contributions expected.

This MAS NMR study appears fully consistent with the diffraction results discussed just before, and especially with the microstructure analysis that highlighted strong strains effects within the $LiVPO_4F_{1-x}O_x$ phases. The analysis of the corresponding ^{7}Li and ^{31}P MAS NMR spectra supports the formation of solid solutions in narrow compositions domains (*i.e.* close in compositions either to LVPF or to LVPO), as NMR signals close but different from those of LVPF and LVPO were observed. These signals are often slightly shifted (of few ppm) but broadened, suggesting a distribution of environments containing either V^{4+} (in LVPF-type phases) or V^{3+} (in

LVPO-type phases) as local defects around the probed nuclei. It is also interesting to mention the case of LVPF-600 which revealed intermediate NMR signals between those typical of LVPF and those typical of LVPO, suggesting that for this sample (*i.e.* in these synthesis conditions) environments more largely mixed in V^{3+} and V^{4+} are formed at the local scale. A study using diffuse reflectance infra-red spectroscopy was performed to definitively support the nature of the defects associated to the presence of V^{4+}, *i.e.* the formation of vanadyl-type bonds.

FTIR

The Mid-IR diffuse reflectance spectra recorded between 450 and 4000 cm^{-1} for all the annealed samples are compared to those of LVPF and LVPO in **Figure 7**. The assignment of the main vibrational bands is given in **Table 3**. The spectra obtained for all the intermediate phases cannot be explained by a simple linear combination of the spectra recorded for the extreme phases $LiVPO_4F$ and $LiVPO_4O$, in good agreement with the results obtained by XRD and NMR which reveal the formation of solid solution type phases $LiVPO_4F_{1-x}O_x$ which are significantly different from $LiVPO_4F$ and $LiVPO_4O$.

In the 3000 - 4000 cm^{-1} region, no contribution was detected in the LVPF spectrum whereas a very broad signal is observed for LVPO. This band is assigned to the adsorbed water stretching vibration in good agreement with the presence of the corresponding H-O-H bending vibration at 1635 cm^{-1} [23]. When the annealing temperature is increased, these two signals appear from 525°C and gradually grow until 700°C. The amount of adsorbed water is thus obviously increased for samples that had been previously treated at higher temperature, despite the decreasing specific surface area of the powder. Actually, this unexpected result can be explained considering the disappearance of the carbon coating with the formation of CO_2 during the annealing in air. That carbon coating would act as a protective layer against the moisture adsorption: without it, the affinity of the material with water is obviously increased.

Otherwise, the vanadyl ($\{V=O\}^{2+}$) stretching vibration mode, in LVPO, is located at 915 cm^{-1} (**Table 3**). This band is not expected in LVPF which is theoretically a V^{3+}-rich fluorophosphate and a vanadyl-free composition. Nevertheless, a tiny peak is observed at 874 cm^{-1}, shifted versus the vanadyl stretching vibration mode observed in LVPO, which could match with the presence of localized vanadyl-type defect in LVPF as already discussed here but also

previously in reference [12]. Moreover, as the temperature is increased, a high wavenumber shift, an increasing intensity and a significant broadening of this vanadyl-type vibration are observed. As already reported, there is a correlation between the length of the V=O bond and the wavenumber of the associated stretching mode [24]. Basically, the shorter is the V=O bond, the higher is the wavenumber. These results obtained in IR are in very good agreement with the structural descriptions reported before, *i.e.* the decrease of the V=O bond length whereas the antagonist V-O bond length increases with temperature (see **Figure 5a**). Furthermore, due to the alternation between shorter and longer V-X distances along the chains with the increasing temperature, the vanadium ions do not occupy anymore the central position of the VO_4X_2 octahedra leading to an increase of the equatorial V-O bond lengths (between 1.97 Å in average for LVPF and 1.99 Å in average for LVPO).

The PO_4 stretching region is located between 950 and 1200 cm^{-1} [24–26]. A single crystallographic site exists for phosphorus in $LiVPO_4F$, whereas two sites are identified in $LiVPO_4O$ due to the lower symmetry (*i.e.* doubling of the unit cell). This is shown by the increase in the number of components in the PO_4 stretching region (**Table 3**). With the increasing temperature, from 375°C, some characteristic vibration bands of $LiVPO_4O$-type appear around 950 and 1165 cm^{-1} and gradually shift and grow in intensity suggesting that LVPF is oxidized to LVPO through the formation of $LiVPO_4F_{1-x}O_x$ phases.

In short, the combination of Synchrotron X-ray powder diffraction, MAS NMR and FTIR spectroscopy allows to demonstrate the formation of vanadyl-type defects in LVPF through thermal treatment in air. Upon increasing temperature, $LiVPO_4F_{1-x}O_x$ phases are formed, in limited composition ranges with x either smaller than 0.1 (of LVPF-type) or higher than 0.9 (of LVPO-type). The influence of these defects on the electrochemical properties will be demonstrated in the following part.

2c. Electrochemical properties versus Lithium

In order to investigate separately the high voltage region (involving the $V^{III}/V^{IV}/V^{V}$ redox couples) and low voltage region (involving $V^{IV}/V^{III}/V^{II}$ redox couples), the pristine materials (*i.e.*

LVPF and LVPO) and all LVPF-T samples were cycled in lithium cells between 3.0 and 1.5 V vs. Li^+/Li and between 3.0 and 4.6 V vs Li^+/Li at a C/50 rate. The resulting galvanostatic and their derivative curves are given in **Figures 8a** and **8b** (for LVPF, LVPO and LVPF-525, and in supplementary information in **Figures S4a** and **S4b** for all the samples). The lithium extraction from $LiVPO_4F$ (*i.e.* here 0.96 Li^+) corresponds to the oxidation of V^{III} to V^{IV} at 4.24 V and then 4.28 V vs Li^+/Li. The transition between the first and the second plateaus occurs at the $Li_{0.67}VPO_4F$ composition. Actually, the charge mechanism is a two steps biphasic process between $LiVPO_4F$, $Li_{0.67}VPO_4F$ and VPO_4F [27]. The following discharge occurs at 4.17 V vs Li^+/Li as a biphasic process between the lithium-free and the fully lithiated phases, with a reversible capacity of 140 mAh/g, and does not involve the intermediate phase. Note that this asymmetric charge/discharge process observed for $LiVPO_4F$ is not fully understood yet. The lithium extraction from the LVPO composition occurs at a lower potential than from LVPF (3.95 V vs Li^+/Li) even if the V^{IV}/V^{V} redox couple is the one involved. Due to the presence of vanadyl bonds the redox couple actually involved is $\{V=O\}^{2+}/\{V=O\}^{3+}$. As synthetized, the reversible capacity of LVPO is about one third of the theoretical one (55 vs. 156 mAh/g). The diffraction and spectroscopic results of this study have highlighted the possibility to substitute partially oxygen for fluorine, and to form partial solid solutions $LiVPO_4F_{1-x}O_x$ by the annealing in air of LVPF. This oxidation induces the appearance of a redox process at around 4.1 V vs. Li^+/Li whose length grows as the annealing temperature is increased. According to the **Figures 8a** and **S4a**, from 525°C, the annealing affects greatly the reversible capacity that decreases, but below this temperature the reversible capacities observed for the LVPF-T samples remain close to that of the pristine LVPF. This decrease in capacity could be explained by deteriorated transport properties for the oxidized compositions due to the sintering of the particles and to the loss of carbon as conductive additive within the active mass during the annealing, as highlighted by SEM images and Raman spectroscopy results. The evolution of the discharge reversible capacity obtained at a C/10 rate (inset in **Figure 8a**) shows a strong and continuous decrease in capacity as the annealing temperature is increased. Furthermore, as described above, the phase diagram observed during the charge of $LiVPO_4F$ presents the formation of an intermediate phase corresponding to the $Li_{0.67}VPO_4F$ composition. The derivative curves given in the **Figures 8b** and

S4b show that the presence of this intermediate phase persists at least until the $LiVPO_4F_{0.90}O_{0.10}$ composition corresponding to the highly fluorinated phase in LVPF-525.

In the low voltage region (*i.e.* 3.0 - 1.5 V vs Li^+/Li), the lithium insertion-extraction into/from LVPF occurs at 1.8 V according to a biphasic process between $LiVPO_4F$ and Li_2VPO_4F involving the V^{III}/V^{II} redox couple (**Figures 8c** and **S4c**). The lithium insertion into LVPO leads to the reduction of V^{IV} to V^{III} and occurs at 2.48 V, 2.31 V then 2.03 V vs Li^+/Li, to reach the $Li_2V^{III}PO_4O$ composition at the end of the discharge with a reversible capacity close to the theoretical one (143 vs. 159 mAh/g). This mechanism involves several intermediate phases $Li_{1.5}VPO_4O$ and $Li_{1.75}VPO_4O$ according to a three steps biphasic mechanism [28]. Coming back to the LVPF-T samples, the electrochemical signature of LVPO appears and grows with the temperature. At 375°C several shoulders appear at 2.45, 2.20 and 2.00 V vs Li^+/Li and the length of the plateau at 1.8 V, related to $LiVPO_4F$-type phase, strongly decreases (as clearly shown by the derivative curves given in the **Figure S4d**). For LVPF-450 and LVPF-525 the electrochemical signature of LVPF disappears whereas XRD revealed the persistence of a fluorine-rich phase at these temperatures. Everything happens as if the $LiVPO_4F$-type phase does not participate in the insertion-extraction processes involved in the low potential region. The strong decrease in capacity in the low voltage domain when fluorine is partially replaced by oxygen in $LiVPO_4F_{1-x}O_x$ even for small values of y, may results from the crystal field.

In our point of view there is a destabilization of V^{II} in an asymmetrical environment (*i.e.* F-V^{II}-O). Indeed, there are significant structural differences between the phases previously mentioned (*i.e.* LVPF, LVPO and the corresponding intercalated compositions), especially concerning the V-X bond length along the chains of VO_4X_2 octahedra. In the V^{III} phases (*i.e.* $LiVPO_4F$ and Li_2VPO_4O) this V-X bond length are almost homogeneous (1.98 Å and 1.95 Å respectively). In $Li_2V^{II}PO_4F$, the V-F are longer (2.12 Å) and also constant because V^{2+} is preferentially stabilized in a symmetrical environment due to its electronic configuration (t_{2g}^3). The insertion of Lithium in a fluorine-rich compound ($V^{(3+\varepsilon)+}$) involves theoretically mainly the reduction of V^{3+} in V^{2+}. Nevertheless, V^{2+} may be destabilized in a distorted environment induced by the presence in its first coordination sphere of oxygen and fluorine along the chain, this could explain why a small amount of oxygen in a $LiVPO_4F$-type phase leads to a strong decrease in capacity. Inversely, the

lithium insertion in an oxygen-rich phase would be promoted as suggested by the comparison of $LiVPO_4F$ and Li_2VPO_4O. Actually, in the pristine material the average oxidation state of vanadium is $V^{(3+\varepsilon)+}$ and the strains highlighted by SXRD measurement would be relaxed thanks to insertion of lithium involving the reduction of V^{IV} to V^{III} and leading to an overall homogenization of the distances V-X along the chains.

The discrepancies observed between this work and the results reported by Ma et al [14] (**Table S2**) may come from small differences in composition, structure and/or morphology for the materials studied. Actually the amount of vanadyle-type defects in $LiVPO_4F$ is a key parameter influencing greatly its electrochemical properties.[12-13] Note for instance that the electrochemical signature given by Ma *et al.* for the pristine material (Figure 10, reference 14) is significantly different from that expected for a stoichiometric composition of $LiVPO_4F$, whereas that reported in this work was fully characterized combining highly sensitive techniques such as NMR IR, and SXRPD and was shown to be stoichiometric.

Conclusion

The oxidation under air at controlled temperature of the promising positive electrode material, $LiVPO_4F$, was investigated in order to get a good knowledge of the different types of defects or compositions which can be formed under synthesis conditions not under control. A combination of high resolution synchrotron powder X-ray diffraction, with infrared and MAS NMR spectroscopies was proved to be the tools of choice to characterize the materials thus formed. Their complex composition, microstructure and defects induced by the annealing treatment impact hugely their electrochemical properties in comparison to those of LVPF and LVPO. Below 450°C, solid solutions $LiVPO_4F_{1-x}O_x$ are formed with less than 10% of oxygen substitution for fluorine and still limited impact on the electrochemical performance at high potential. Above 450°C the effect is drastic, moving from a LVPF-type electrochemical signature to that of LVPO-type, with a decreasing average discharge potential, a larger hysteresis between the charge and the discharge, a decrease of the reversible capacity etc. In the low voltage region, the effect of the oxygen defects is even more pronounced, everything happens as if the presence of vanadyl-type defects would prevent the formation of V^{2+} during lithium

intercalation in the mixed valence V^{III}/V^{IV} pristine materials, $LiVPO_4F_{1-x}O_x$: very rapidly, already with a small amount of oxygen substitution for fluorine, only the $LiVPO_4O$'s electrochemical signature is detected.

This work allows providing a description of the nature of the defects or of the derived compositions which can be obtained when the synthesis conditions of $LiVPO_4F$ are not perfectly controlled, versus the oxygen content during the thermal treatment or the cooling. Furthermore, this study reveals that the versatility of the vanadium chemistry with a large number of stable oxidations states (from V^{2+} to V^{5+}), but stabilized in very different environments (from very regular to very distorted ones), opens the road to the formation of new materials, whose structures and electrochemical activity can be complex to control due to the strains imposed by the crystal field.

Acknowledgment

The authors thank Philippe Dagault, Cathy Denage, Laetitia Etienne, and Eric Lebraud at ICMCB and Matthieu Courty at LRCS for technical assistance, François Weill and Sonia Buffière at ICMCB for the microscopy experiments, as well as ALBA (Barcelona, Spain) for Synchrotron X-ray diffraction experiments on MSPD beamline (proposal number 2015021236). The authors also acknowledge FEDER, the Région Haut-de-France and the RS2E Network for the funding of EB's PhD thesis, as well as the financial support of Région Nouvelle Aquitaine and of the French National Research Agency (STORE-EX Labex Project ANR-10-LABX-76-01 and HIPOLITE Progelec project ANR-12-PRGE-0005-02).

References

(1) Manthiram, A.; Goodenough, J. B. Lithium Insertion into $Fe_2(MO_4)_3$ Frameworks: Comparison of M = W with M = MO. *J. Solid State Chem.* **1987**, *71*, 349–360.

(2) Masquelier, C.; Croguennec, L. Polyanionic (phosphates, Silicates, Sulfates) Frameworks as Electrode Materials for Rechargeable Li (or Na) Batteries. *Chem. Rev.* **2013**, *113*, 6552–6591.

(3) Whittingham, M. S. Quest for Nonaqueous Multivalent Secondary Batteries: Magnesium and Beyond. *Chem. Rev.* **2014**.

(4) Rousse, G.; Tarascon, J. M. Sulfate-Based Polyanionic Compounds for Li-Ion Batteries: Synthesis, Crystal Chemistry, and Electrochemistry Aspects. *Chem. Mater.* **2014**, *26*, 394–406.

(5) Marx, N.; Croquennec, L.; Cartier, D.; Wattiaux, A.; Le Cras, F.; Suard, E.; Delmas, C. The Structure of Tavorite $LiFePO_4(OH)$ from Diffraction and GGA + U Studies and Its Preliminary Electrochemical Characterization. *Dalton Trans.* **2010**, *39*, 5108–5116.

(6) Recham, N.; Chotard, J.-N.; Jumas, J.-C.; Laffont, L.; Armand, M.; Tarascon, J.-M. Ionothermal Synthesis of Li-Based Fluorophosphates Electrodes †. *Chem. Mater.* **2010**, *22*, 1142–1148.

(7) Barker, J.; Saidi, M. Y.; Swoyer, J. L. Electrochemical Insertion Properties of the Novel Lithium Vanadium Fluorophosphate, $LiVPO_4F$. *J. Electrochem. Soc.* **2003**, *150*, A1394.

(8) Ateba Mba, J.-M.; Masquelier, C.; Suard, E.; Croguennec, L. Synthesis and Crystallographic Study of Homeotypic $LiVPO_4F$ and $LiVPO_4O$. *Chem. Mater.* **2012**, *24*, 1223–1234.

(9) Kim, M.; Lee, S.; Kang, B. Fast-Rate Capable Electrode Material with Higher Energy Density than LiFePO 4 : 4.2V $LiVPO_4F$ Synthesized by Scalable Single-Step Solid-State Reaction. *Adv. Sci.* **2015**, 1–9.

(10) Zheng, J.; Zhang, B.; Yang, Z. Novel Synthesis of $LiVPO_4F$ Cathode Material by Chemical Lithiation and Postannealing. *J. Power Sources* **2012**, *202*, 380–383.

(11) Xiao, P. F.; Lai, M. O.; Lu, L. Transport and Electrochemical Properties of High Potential Tavorite LiVPO4F. *Solid State Ionics* **2013**, *242*, 10–19.

(12) Messinger, R. J.; Ménétrier, M.; Salager, E.; Boulineau, A.; Duttine, M.; Carlier, D.; Ateba Mba, J.-M.; Croguennec, L.; Masquelier, C.; Massiot, D.; et al. Revealing Defects in Crystalline Lithium-Ion Battery Electrodes by Solid-State NMR: Applications to $LiVPO_4F$. *Chem. Mater.* **2015**, *27*, 5212–5221.

(13) Ateba Mba, J.-M. PhD Thesis,. *Univ. Bordeaux,* **2013**.

(14) Ma, R.; Shao, L.; Wu, K.; Shui, M.; Wang, D.; Long, N.; Ren, Y.; Shu, J. Effects of Oxidation on Structure and Performance of $LiVPO_4F$ as Cathode Material for Lithium-Ion Batteries. *J. Power Sources* **2014**, *248*, 874–885.

(15) Fauth, F.; Peral, I.; Popescu, C.; Knapp, M. The New Material Science Powder Diffraction Beamline at ALBA Synchrotron. *Powder Diffr.* **2013**, *28*, 360–370.

(16) Rodriguez-carvajal, J. Recent Advances in Magnetic Structure Determination by Neutron Powder Diffraction. *Phys. B* **1993**, *192*, 55–69.

(17) Stephens, P. W. Phenomenological Model of Anisotropic Peak Broadening in Powder Diffraction. *J. Appl. Crystallogr.* **1999**, *32*, 281–289.

(18) Rodríquez-Carvajal, J.; Roisnel, T. Line Broadening Analysis Using FullProf: Determination of Microstructural Properties. *Mater. Sci. Forum* **2004**, *443-444*, 123–126.

(19) Onoda, M.; Ishibashi, T. Phase Transition and Spin Dynamics of the $LiVFPO_4$ Insertion Electrode with the S = 1 Linear Chain and the Development of F – O Mixed System. **2015**, *044802*, 1–5.

(20) Ellis, B. L.; Ramesh, T. N.; Davis, L. J. M.; Goward, G. R.; Nazar, L. F. Structure and Electrochemistry of Two-Electron Redox Couples in Lithium Metal Fluorophosphates Based on the Tavorite Structure. *Chem. Mater.* **2011**, *23*, 5138–5148.

(21) Bertini, I.; Luchinat, C.; Parigi, G. Magnetic Susceptibility in Paramagnetic NMR. *Prog. Nucl. Magn. Reson. Spectrosc.* **2002**, *40*, 249–273.

(22) Bamine, T.; Duttine, M.; Boucher, F.; Messinger, R. J.; Salager, E.; Deschamps, M.; Ateba Mba, J.-M.; Masquelier, C.; Croguennec, L.; Ménétrier, M.; et al. Understanding the Defect in $LiVPO_4F$: A Combined NMR and DFT Calculations Study. *Abstr. LIBD 2015* **2015**, 5–6.

(23) Nakamoto, K. *Infrared and Raman Spectra of Inorganic and Coordination Compounds. Part B: Applications in Coordination, Organometallic, and Bioinorganic Chemistry*; John Wiley & Sons, Inc., 1997; 161.

(24) Harrison, K. L.; Manthiram, A. Microwave-Assisted Solvothermal Synthesis and Characterization of Various Polymorphs of $LiVOPO_4$. *chem. mater.* **2013**, *25*, 1751–1760.

(25) Marx, N.; Croguennec, L.; Carlier, D.; Bourgeois, L.; Kubiak, P.; Cras, F. Le; Delmas, C. Structural and Electrochemical Study of a New Crystalline Hydrated Iron(III) Phosphate

$FePO_4 \cdot H_2O$ Obtained from $LiFePO_4(OH)$ by Ion Exchange. *Chem. Mater.* **2010**, *22*, 1854–1861.

(26) Boivin, E.; Chotard, J.-N.; Ménétrier, M.; Bourgeois, L.; Bamine, T.; Carlier, D.; Fauth, F.; Suard, E.; Masquelier, C.; Croguennec, L. Structural and Electrochemical Studies of a New Tavorite Composition $LiVPO_4OH$. *J. Mater. Chem. A* **2016**, *4*, 11030–11045.

(27) Ateba Mba, J.-M.; Croguennec, L.; Basir, N. I.; Barker, J.; Masquelier, C. Lithium Insertion or Extraction From/into Tavorite-Type LiVPO4F: An In Situ X-Ray Diffraction Study. *J. Electrochem. Soc.* **2012**, *159*, A1171–A1175.

(28) Bianchini, M.; Ateba Mba, J.-M.; Dagault, P.; Bogdan, E.; Carlier, D.; Suard, E.; Masquelier, C.; Croguennec, L. Multiple Phases in the E-VPO4O–LiVPO4O–Li2VPO4O System: A Combined Solid State Electrochemistry and Diffraction Structural Study. *J. Mater. Chem. A* **2014**, *2*, 10182.

(29) Hardcastle, F. D.; Wachs, I. E. Determination of Vanadium-Oxygen Bond Distances and Bond Orders by Raman Spectroscopy. *J. Phys. Chem. C* **1991**, *95*, 5031–5041.

Table captions

***Table 1**: Results of CHNS and ICP-OES chemical analyses carried out on all samples. Their color varies according to the weight percentage of carbon and to the oxidation state of vanadium. The average particle sizes are obtained thanks to SEM images given in inset at the figure 3.*

***Table 2**: Summary of the parameters determined for each sample from the Rietveld refinement of its Synchrotron powder X-ray diffraction pattern. The weight percentage associated to each phase contained in the samples (1 or 2), their V/Z unit cell volumes and the corresponding R_{Bragg} reliability factor are listed in the first three columns. The vanadium average oxidation state in each phase and the global composition of each sample were obtained taking into account the Vegard's law applied to the unit cell volume. The shorter V-X bond and the antagonist longer V-X bond along the chains $[X\text{-}VO_4\text{-}X]_n$ are also listed. The four last columns summarize the microstructure analysis. The width of microstrains' distribution along the [100], [010], [001] directions and in average for all [hkl] directions ($\varepsilon = \Delta d_{hkl}/d_{hkl}$) and the crystallites domain sizes are given (* means no size effect induced broadening detected).*

***Table 3**: Wavenumbers and assignment of the main vibration bands observed by diffuse reflectance IR spectroscopy.*

***Table 1**:*

Samples	colors	CHNS	ICP-OES			Particle
		C (w%)	Li/V	Li/P	V/P	Sizes (nm)
LVPF	Black	5.65	0.98	1.02	1.04	300 – 600
LVPF-375	Black	4.29	1.02	1.01	0.99	300 – 600
LVPF-450	Dark grey	1.09	0.99	1.01	1.02	300 – 600
LVPF-525	Brown	0.22	0.97	0.99	1.03	500 – 1000
LVPF-600	Brown	/	1.03	1.06	1.03	500 – 2000
LVPF-700	Dark green	/	1.05	1.04	0.99	1000 – 5000
LVPO	Green	/	0.99	1.02	1.03	500 – 1000

***Table 2**:*

	# phase	R_{Bragg} (%)	wt.%	V/Z (Å^3)	Vanadium average oxidation state	Global composition	Distances along the chains (Å)		Width of microstrains distribution ε_{hkl} (%) along				Crystallites' domain size D (nm)
							the longer V-X	the shorter V-X	[100]	[010]	[001]	In average, <hkl>	
LVPF	1	3.72	100	87.18(1)	3	$LiVPO_4F$	2.00(3)	1.96(3)	0.12	0.09	0.07	0.13	256.2
LVPF-375	1	2.53	100	87.12(1)	3.04	$LiVPO_4O_{0.04}F_{0.96}$	2.00(3)	1.96(3)	0.16	0.19	0.17	0.20	466.1
LVPF-450	1	2.61	100	87.05(1)	3.08	$LiVPO_4O_{0.08}F_{0.92}$	2.02(3)	1.93(3)	0.20	0.20	0.18	0.24	607.4
LVPF-525	1	3.34	35(1)	87.01(2)	3.10	$LiVPO_4O_{0.65}F_{0.35}$	2.04(3)	1.85(3)	0.23	0.31	0.25	0.33	173.8
	2	2.14	65(1)	85.63(2)	3.92		2.08 (3)	1.78(3)	0.64	0.72	0.40	0.53	227.1
LVPF-600	1	3.14	47(2)	85.69(2)	3.89	$LiVPO_4O_{0.93}F_{0.07}$	2.04(3)	1.84(3)	0.32	0.27	0.24	0.27	*
	2	2.64	53(2)	85.56(2)	3.97		2.08(3)	1.73(3)	0.33	0.40	0.33	0.35	767.6
LVPF-700	1	3.21	41(2)	85.58(1)	3.96	$LiVPO_4O_{0.98}F_{0.02}$	2.15(3)	1.72(3)	0.23	0.19	0.23	0.21	*
	2	2.15	59(2)	85.52(2)	3.99		2.25(3)	1.60(3)	0.24	0.23	0.24	0.23	1276.0
LVPO	1	2.07	100	85.51(1)	4	$LiVPO_4O$	2.24(3)	1.63(3)	/	/	/	/	/

***Table 3**:*

wavenumber (cm^{-1})							assignment	ref
LVPF	**LVPF-375**	**LVPF-450**	**LVPF-525**	**LVPF-600**	**LVPF-700**	**LVPO**		
/	/	/	3400	3400	3400	3400	$\nu_{H\text{-}O\text{-}H}$	[23]
/	/	/	1650	1650	1650	1650	$\delta_{H\text{-}O\text{-}H}$	[23]
/	/	1163	1165	1166	1165	1165	ν_{PO4}	[24,26]
1120	1121	1113	1104	1104	1104	1103	ν_{PO4}	[24–26]
1051	1048	1051	1050	1055	1056	1056	ν_{PO4}	[24–26]
1007	1007	1006	1006	1001	998	998	ν_{PO4}	[24–26]
/	/	953	953	951	952	953	ν_{PO4}	[24,26]
874	877	889	896	895	912	915	$\nu_{V=O}$	[26,29]

Figure captions

***Figure 1**: Rietveld refinement of the pristine LVPF structure based on Synchrotron powder X-ray diffraction data. The observed intensities are plotted as red points, the theoretical Bragg positions are plotted as blue marks, calculated intensities and the difference between observed and calculated intensities are plotted as black lines.*

***Figure 2**: TGA curve obtained under air for the pristine LVPF as function of time and plotted as a blue line and the corresponding temperature vs time curve plotted as a red line. The heating/cooling rate is ± 5°C/min and the temperature plateau is maintained during 30 minutes.*

***Figure 3**: Synchrotron XRD patterns of the pristine materials (LVPF and LVPO) and the annealed samples (LVPF-375, LVPF-450, LVPF-525, LVPF-600 and LVPF-700). Corresponding SEM images are shown in inset.*

***Figure 4**: Rietveld refinements obtained for the samples LVPF-450 (a) and LVPF-525 (b) taking into account the structural model of $LiVPO_4O$. The observed intensities are plotted as red points, the theoretical Bragg positions are plotted as blue ($LiVPO_4F$-type phase) or purple ($LiVPO_4O$-type phase) marks, calculated intensities and the difference between observed and calculated intensities are plotted as black lines. In inset, a zoom between 11 and 18.5° in which the contribution of each phase is represented.*

***Figure 5**: (a) evolution of the shorter and longer V-X distances along the $[X\text{-}VO_4\text{-}X]_n$ chains as function of the vanadium oxidation state. The empty circles represent the long V-X distances and full circles the short V-X distances. (b) The width of the microstrains' distribution along [100] (square), [010] (triangles) and [001] (circles) directions, and the average on all [hkl] (stars) directions.*

***Figure 6:** ^{7}Li (a) and ^{31}P (b) normalized (according to the mass of the sample) NMR spectra of LVPF, LVPF-375, LVPF-450, LVPF-525, LVPF-600, LVPF-700 and LVPO. In inset, zooms of the isotropic signals associated to the different contributions. The isotropic peaks are noted by #, their spinning side bands by * and additional contributions by ∇. The contributions which can be assigned to a ^{31}P in interaction with both V^{3+} and V^{4+} cations are noted by | .*

***Figure 7:** Diffuse reflectance infrared spectra of LVPF, LVPO and the LVPF-T samples in the 475 - 3800 cm^{-1} range and, in inset, the 800 - 1200 cm^{-1} region assigned to the stretching vibrations of PO_4 groups and V=O bonds.*

***Figure 8**:* Galvanostatic curves obtained versus Lithium at a C/50 rate for LVPF, LVPO and LVPF-525: (a) in the high voltage domain (*i.e.* between 3.0 and 4.6 V *vs* Li^+/Li) and (c) in the low voltage domain (1.5 - 3.0 V *vs* Li^+/Li). The corresponding derivative curves are given in (b) and

(d). The evolution of the discharge capacity the corresponding samples at C/10 is given in inset of (a).

Figure 1

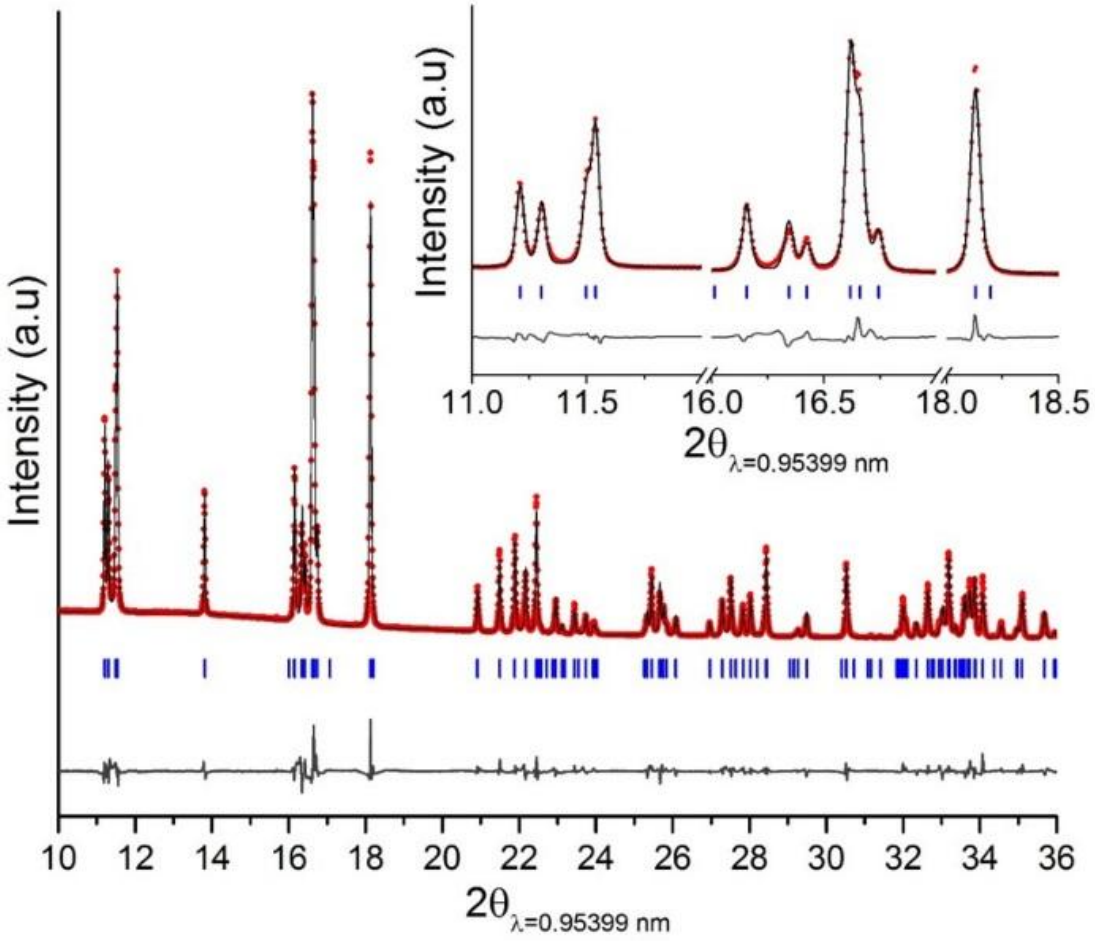
Intensity (a.u)
10
12
14
16
18
20
22
24
26
28
30
32
34
36
2θ λ=0.95399 nm
Intensity (a.u)
11.0
11.5
16.0
16.5
18.0
18.5
2θ λ=0.95399 nm

Figure 2

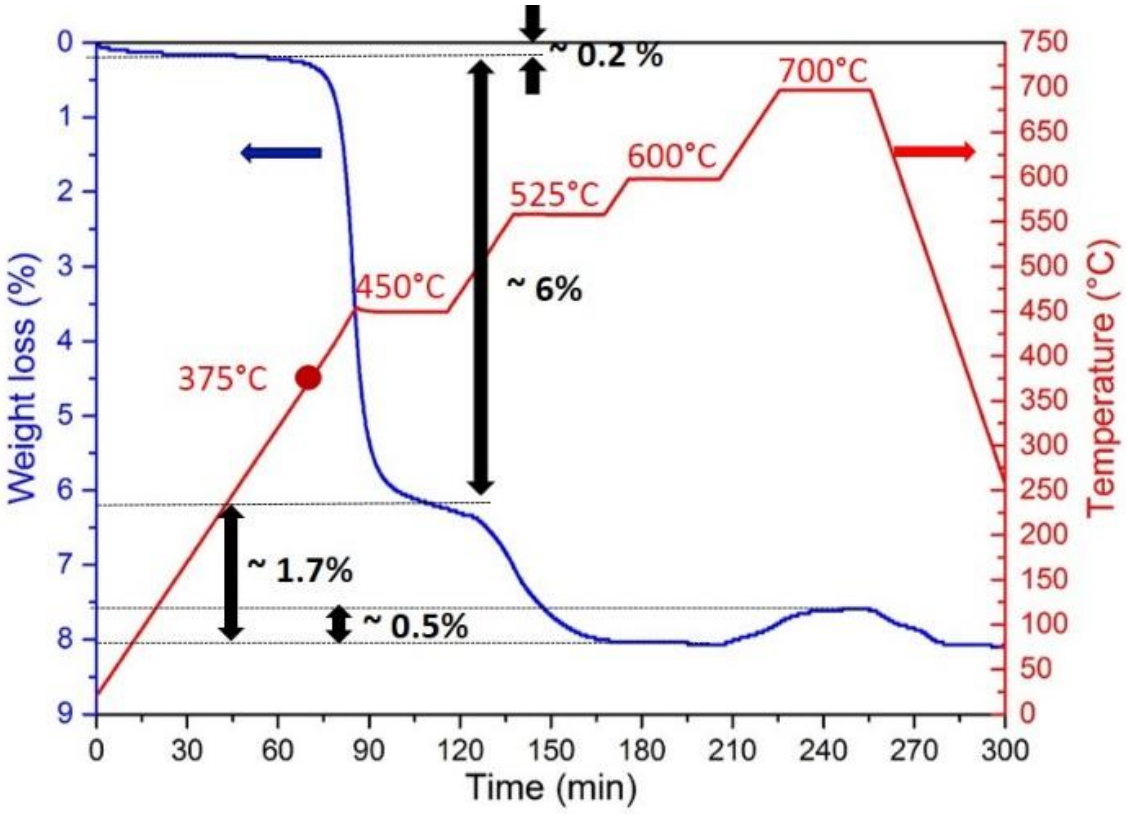
~ 0.2 %
700°C
600°C
525°C
450°C
375°C
~ 6%
~ 1.7%
~ 0.5%
Weight loss (%)
Temperature (°C)
Time (min)
0
1
2
3
4
5
6
7
8
9
750
700
650
600
550
500
450
400
350
300
250
200
150
100
50
0
0
30
60
90
120
150
180
210
240
270
300

Figure 3

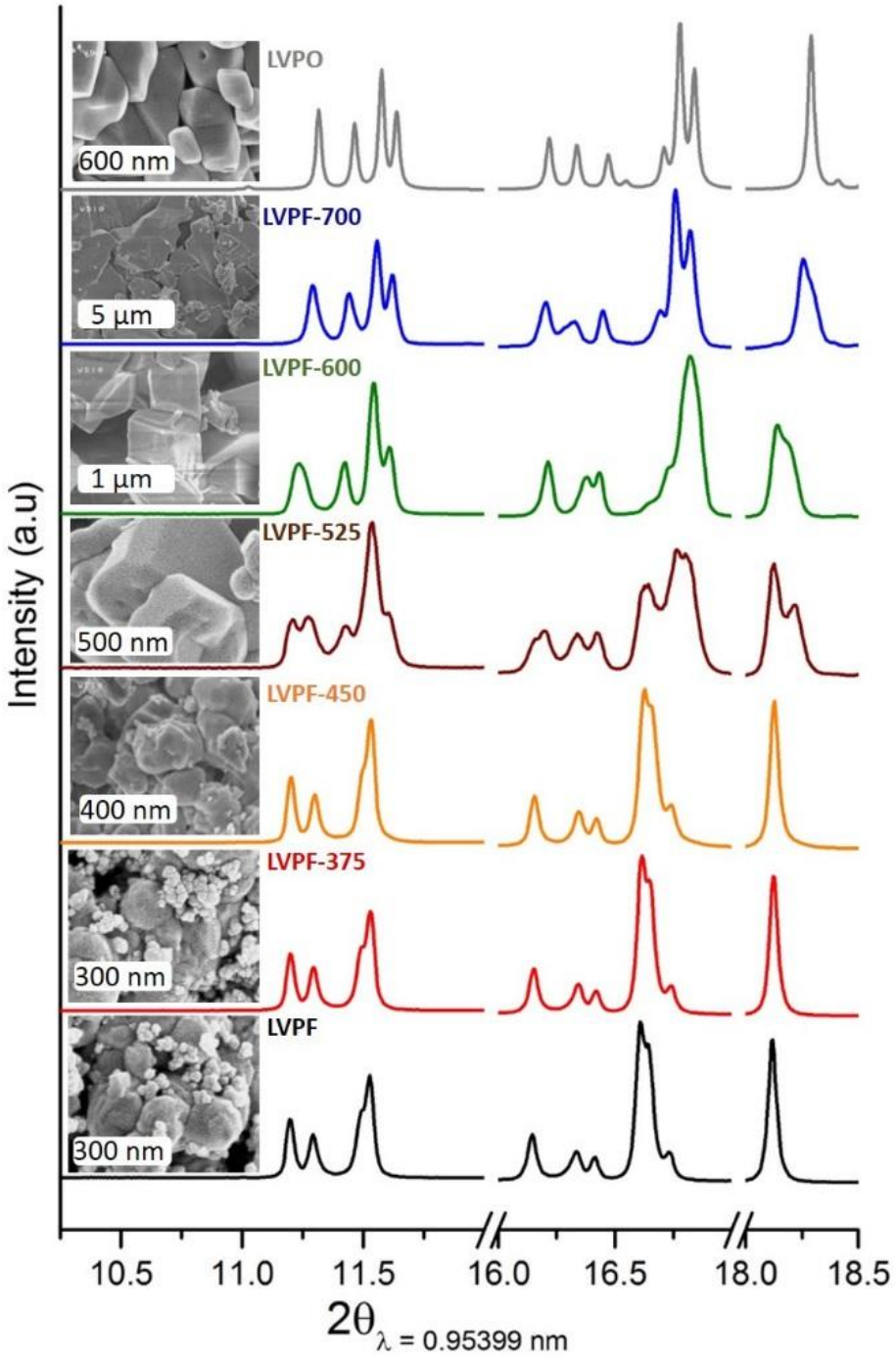
LVPO
600 nm
LVPF-700
5 µm
LVPF-600
1 µm
LVPF-525
500 nm
LVPF-450
400 nm
LVPF-375
300 nm
LVPF
300 nm
Intensity (a.u)
10.5
11.0
11.5
16.0
16.5
18.0
18.5
2θ
λ = 0.95399 nm

Figure 4

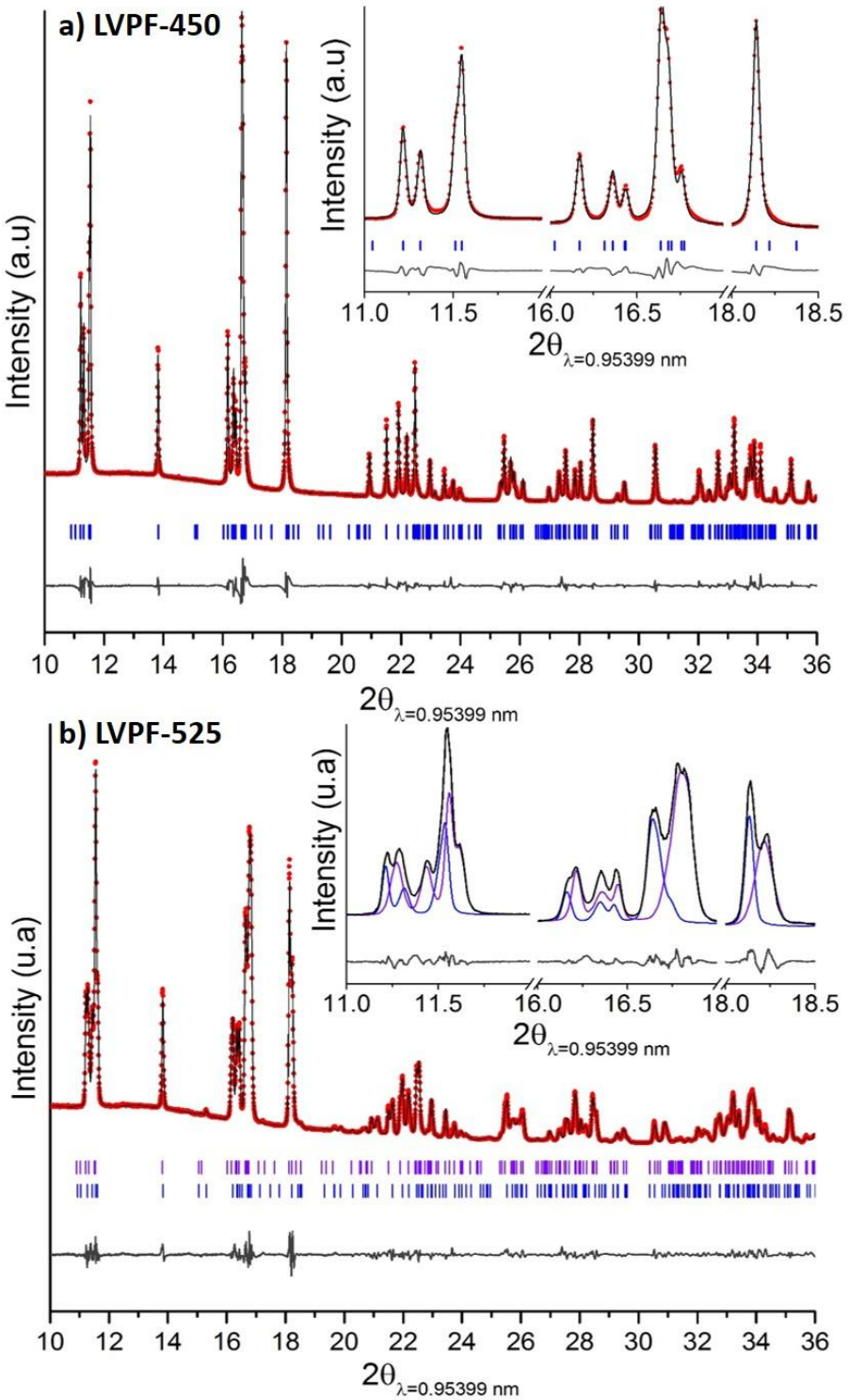
a) LVPF-450
Intensity (a.u)
Intensity (a.u)
11.0
11.5
16.0
16.5
18.0
18.5
2θ λ=0.95399 nm
10
12
14
16
18
20
22
24
26
28
30
32
34
36
2θ λ=0.95399 nm
b) LVPF-525
Intensity (u.a)
Intensity (u.a)
11.0
11.5
16.0
16.5
18.0
18.5
2θ λ=0.95399 nm
10
12
14
16
18
20
22
24
26
28
30
32
34
36
2θ λ=0.95399 nm

Figure 5

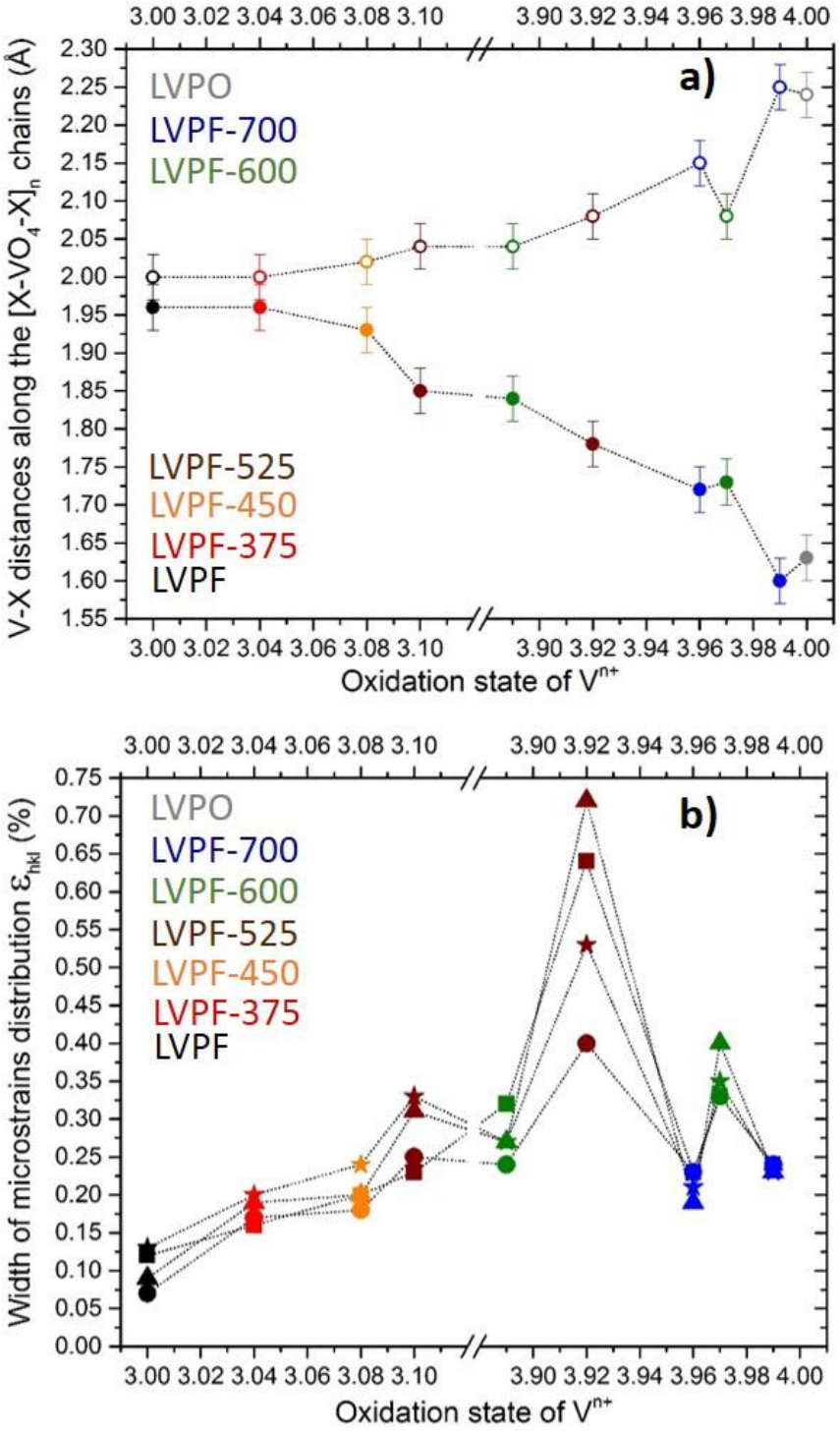
a)
LVPO
LVPF-700
LVPF-600
LVPF-525
LVPF-450
LVPF-375
LVPF
V-X distances along the [X-VO4-X]n chains (Å)
Oxidation state of V^n+
b)
LVPO
LVPF-700
LVPF-600
LVPF-525
LVPF-450
LVPF-375
LVPF
Width of microstrains distribution ε_hkl (%)
Oxidation state of V^n+

Figure 6

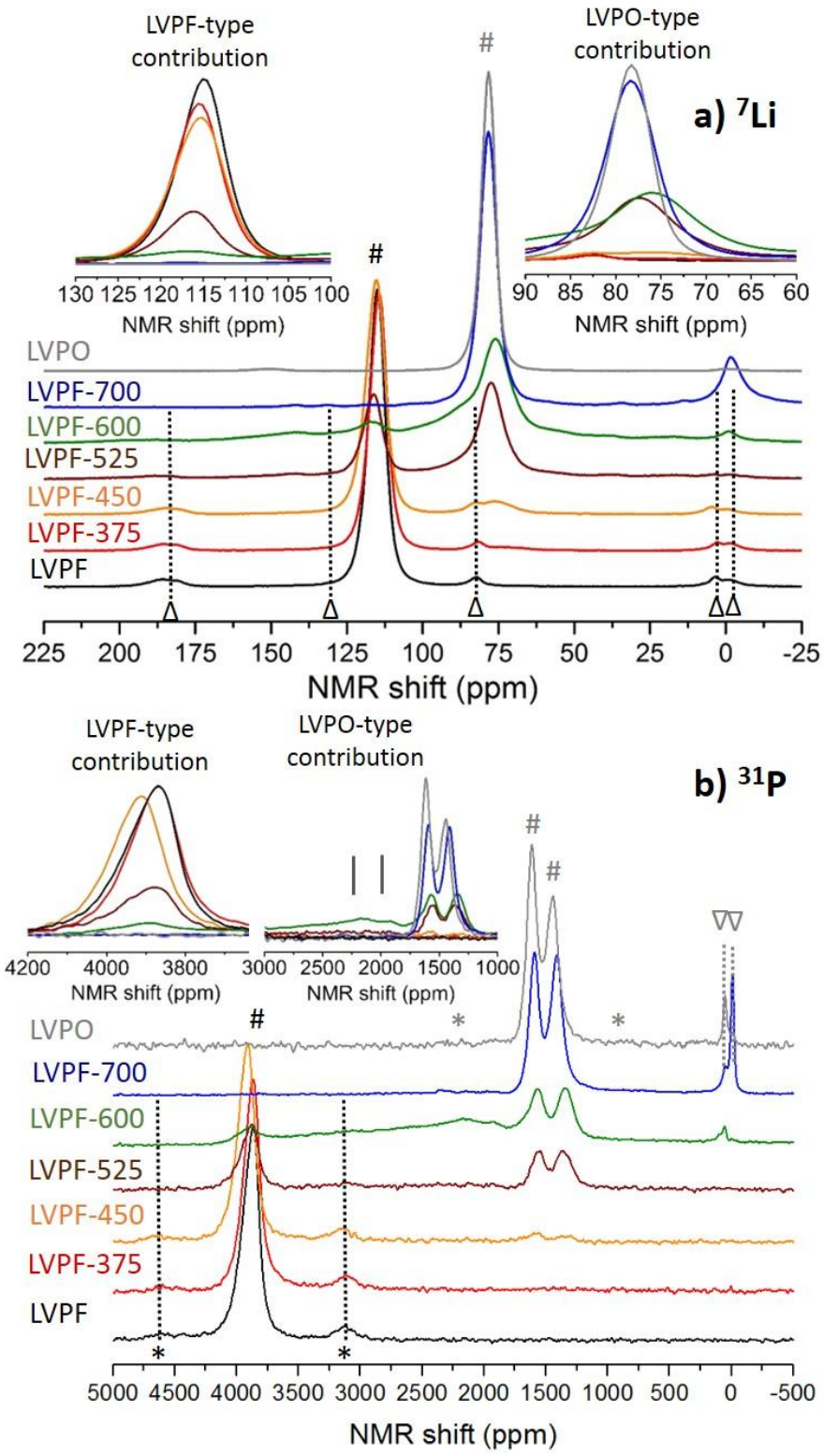
LVPF-type contribution
LVPO-type contribution
a) 7Li
#
130 125 120 115 110 105 100
NMR shift (ppm)
90 85 80 75 70 65 60
NMR shift (ppm)
LVPO
LVPF-700
LVPF-600
LVPF-525
LVPF-450
LVPF-375
LVPF
225 200 175 150 125 100 75 50 25 0 -25
NMR shift (ppm)
LVPF-type contribution
LVPO-type contribution
b) 31P
4200 4000 3800
NMR shift (ppm)
3000 2500 2000 1500 1000
NMR shift (ppm)
*
5000 4500 4000 3500 3000 2500 2000 1500 1000 500 0 -500
NMR shift (ppm)

Figure 7

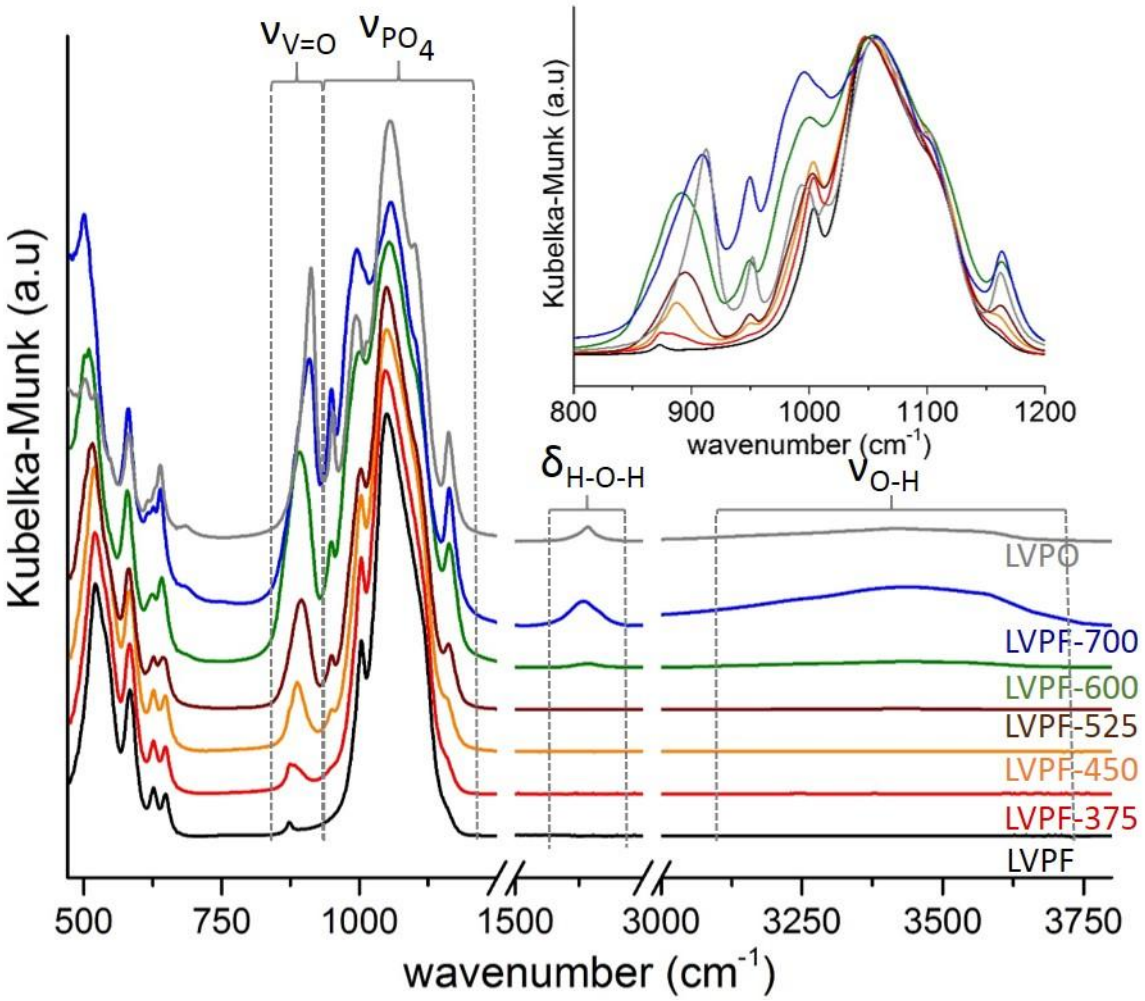
Kubelka-Munk (a.u)
$\nu_{V=O}$
ν_{PO_4}
δ_{H-O-H}
ν_{O-H}
LVPO
LVPF-700
LVPF-600
LVPF-525
LVPF-450
LVPF-375
LVPF
500
750
1000
1500
3000
3250
3500
3750
wavenumber (cm^{-1})
Kubelka-Munk (a.u)
800
900
1000
1100
1200
wavenumber (cm^{-1})

Figure 8

Figure to be included in the text as a double columns figure

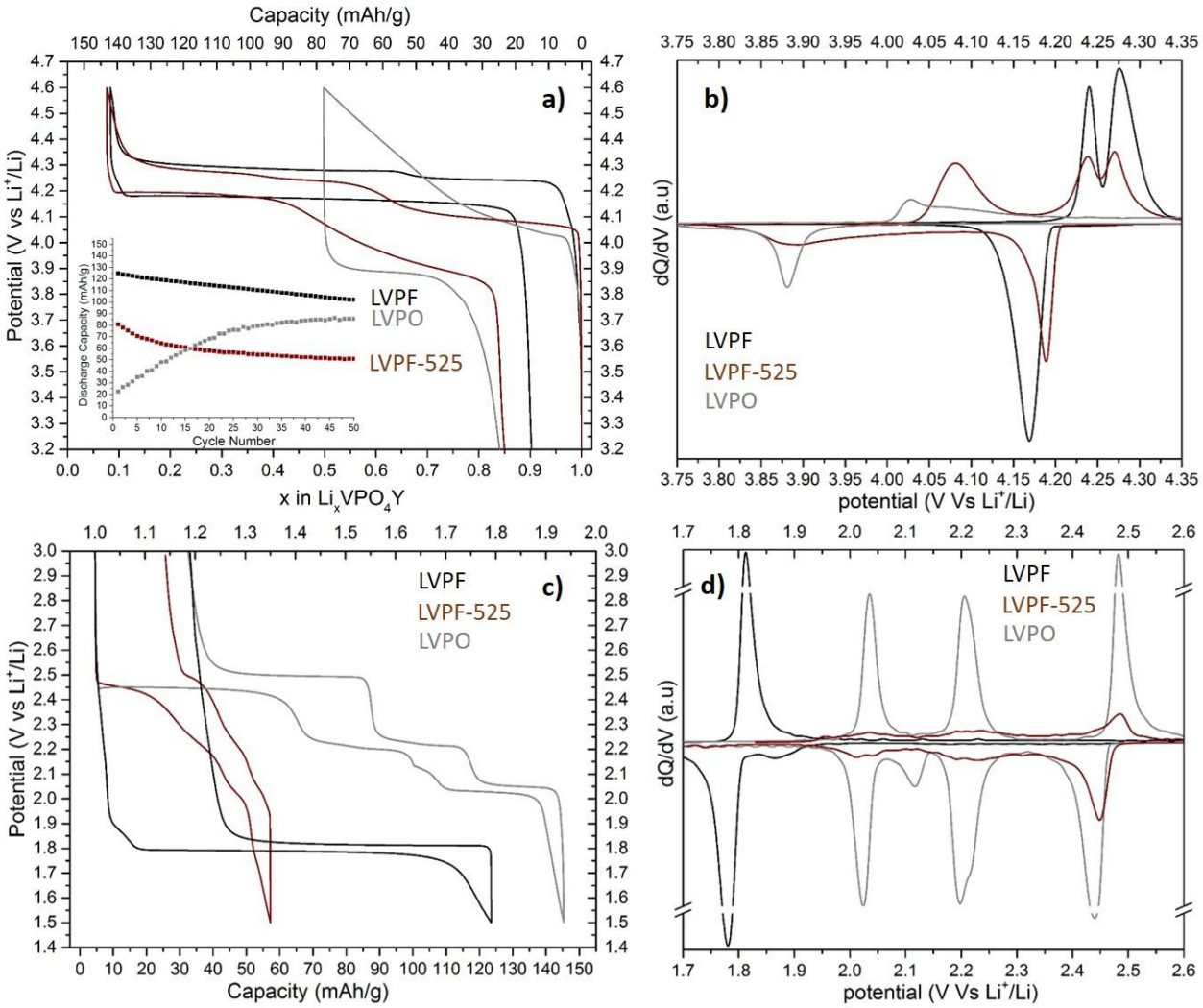

TOC graphic

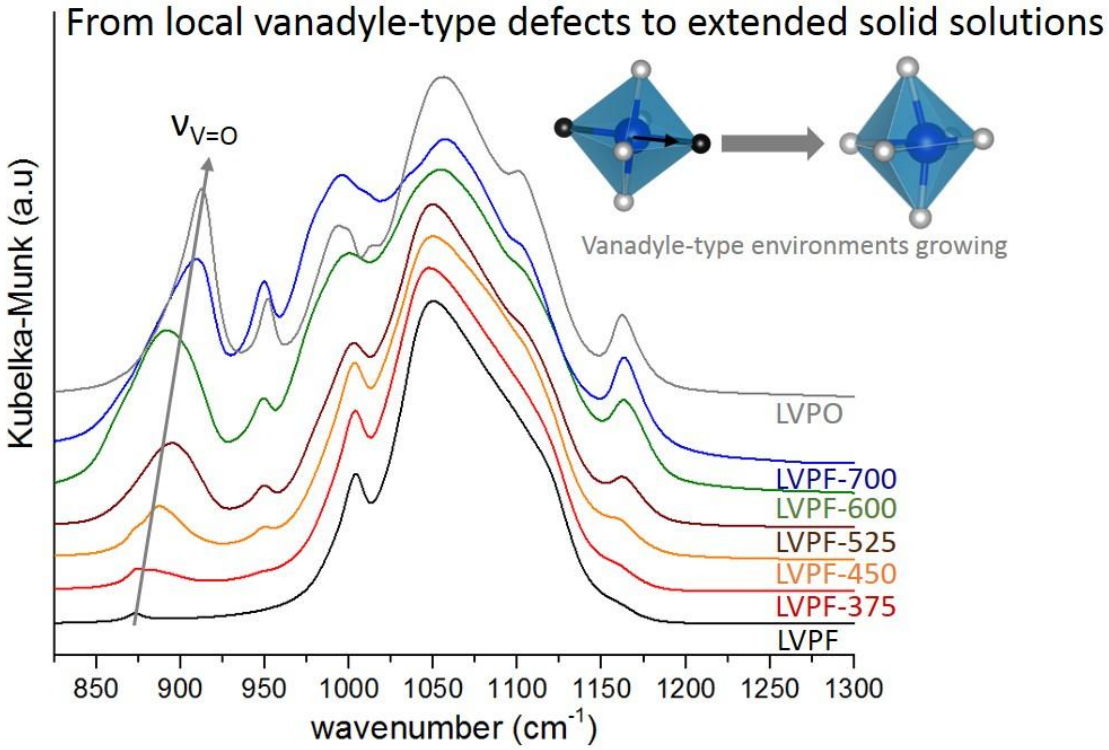
From local vanadyle-type defects to extended solid solutions
$\nu_{V=O}$
Vanadyle-type environments growing
Kubelka-Munk (a.u)
LVPO
LVPF-700
LVPF-600
LVPF-525
LVPF-450
LVPF-375
LVPF
850
900
950
1000
1050
1100
1150
1200
1250
1300
wavenumber (cm^{-1})